Title

Novel Spin—Orbit Torque Generation at Room Temperature in an All-Oxide Epitaxial La0.7Sr0.3MnO3/SrIrO3 System



Journal

Advanced Materials, 33(24)

ISSN

0935-9648

Authors

Huang, Xiaoxi
Sayed, Shehrin
Mittelstaedt, Joseph
et al.

Publication Date

2021-06-01

DOI

10.1002/adma.202008269

# Novel spin-orbit torque generation at room temperature in an all-oxide epitaxial $La_{0.7}Sr_{0.3}MnO_3/SrIrO_3$ system

Xiaoxi Huang[1*], Shehrin Sayed[2], Joseph Mittelstaedt[3], Sandhya Susarla[6], Saba Karimeddiny[3], Lucas Caretta[1], Hongrui Zhang[1], Vladmir A. Stoica[8], Tanay Gosavi[5], Farzad Mahfouzi[9], Qilong Sun[9], Peter Ercius[10], Nicholas Kioussis[9], Sayeef Salahuddin[2], Daniel C. Ralph[3,4], Ramamoorthy Ramesh[1,6,7*]

[1]Department of Materials Science and Engineering, University of California, Berkeley, CA 94720, USA

[2]Department of Electrical Engineering and Computer Science, University of California, Berkeley, CA 94720, USA

[3]Department of Physics, Cornell University, Ithaca, NY 14853, USA

[4]Kavli Institute at Cornell for Nanoscale Science, Ithaca, NY 14853, USA

[5]Components Research, Intel Corporation, Hillsboro, OR 97124, USA

[6]Materials Sciences Division, Lawrence Berkeley National Laboratory, CA 94720, USA

[7]Department of Physics, University of California, Berkeley, CA 94720, USA

[8]Department of Materials Science and Engineering, Pennsylvania State University, University Park, PA 16802, USA

[9]Department of Physics, California State University Northridge, Northridge, CA 91330, USA

[10]National Center for Electron Microscopy, Lawrence Berkeley National Laboratory, Berkeley, CA 94720, USA

*Author to whom correspondence should be addressed. Electronic mail: xiaoxi_huang@berkeley.edu, rramesh@berkeley.edu

**Abstract**: Spin-orbit torques (SOT) that arise from materials with large spin-orbit coupling offer a new pathway for energy-efficient and fast magnetic information storage. SOTs in conventional heavy metals and topological insulators have been explored extensively, while 5*d* transition metal oxides, which also host ions with strong spin-orbit coupling, are a relatively new territory in the field of spintronics. An all-oxide, $SrTiO_3$ (STO)// $La_{0.7}Sr_{0.3}MnO_3$ (LSMO)/ $SrIrO_3$ (SIO) heterostructure with lattice-matched crystal structure has been synthesized, exhibiting an epitaxial and atomically-sharp interface between the ferromagnetic LSMO and the high spin-orbit-coupled metal SIO. We use spin-torque ferromagnetic resonance (ST-FMR) to probe the effective magnetization and the SOT efficiency in LSMO/SIO heterostructures grown on STO substrates. Remarkably, epitaxial LSMO/SIO exhibits a large SOT efficiency, $\xi_{||}$ = 1, while retaining a reasonably low shunting factor and increasing the effective magnetization of

LSMO by ~50%. Our findings highlight the significance of epitaxy as a powerful tool to achieve a high SOT efficiency, explore the rich physics at the epitaxial interface, and open up a new pathway for designing next-generation energy-efficient spintronic devices.

## Main text

Efficient electrical manipulation of magnetism is an ongoing pursuit for applications in next-generation information storage and logic functions. One promising pathway is to utilize current-induced spin torques originating from spin-orbit coupling (SOC)[1-3], such as the bulk spin Hall effect (SHE)[4-6]or the interfacial Rashba-Edelstein effect (REE)[7-9], where a charge current passed through a SOC metal generates a spin torque on an adjacent ferromagnet (FM). The key to realizing energy-efficient spin-orbit torque (SOT)-based switching of FM's is to maximize the anti-damping SOT efficiency (per unit current density) $\xi_{||} = \theta_{||} T_{\mathrm{int}}$ , where $\theta_{||}$ is the spin Hall ratio and $T_{\mathrm{int}}$ is an interfacial spin transparency factor. Consequently, there is tremendous on-going research focused on achieving such large SOT efficiencies by using materials with large SOC, such as elemental heavy metals (HM) [5, 6, 10-13], topological insulators (TI) [14-17] with spin momentum locked interface states, and two-dimensional electron gases (2DEG) at oxide interfaces [18-20]. However, in HM's SOT efficiencies are typically below 0.5 [21, 22], and in TI/FM and 2DEG systems the high resistivity of the spin Hall material causes current shunting through the magnet that compromises the overall efficiency per unit applied current [23, 24]. Here, we show that model epitaxial all-oxide heterostructures can achieve SOT efficiencies on par with some TI materials at room temperature[9], while allowing lower-resistivity SOC layers and high-resistivity oxide FMs that together decrease unwanted current shunting compared to TI or 2DEG/metallic FM structures. Moreover, we find an unusual dependence of the oxide FM magnetic anisotropy on the thickness of the oxide SOC material, highlighting the rich physics in correlated oxide spintronics systems.

Complex oxides, displaying a strong interplay between charge, spin, orbital, and lattice degrees of freedom, offer a scientifically-rich platform for both fundamental and application-oriented research. Their properties range from high-temperature superconductivity in cuprates, colossal magnetoresistance in doped manganites[25], and more recently, exotic band structure effects in perovskite iridates[26]. Moreover, the sensitivity of complex oxides to epitaxial strain [27], interface chemistry, and crystal orientation provide additional degrees of freedom in tuning the electronic and magnetic structure and SOC effects. In particular, 5*d* transition metal oxides (TMO), with strong SOC and electron-electron correlation, give rise to intriguing fundamental physics, ranging from nontrivial quantum phases [28-30] to magnetic anisotropy manipulation[31] and intrinsic charge-spin interconversion[32-35]. However, despite this rich physics, in the few room temperature studies on charge-spin interconversion in 5*d* TMOs, the adjacent FM metal has typically been a non-epitaxial metal, such as $SrIrO_3$ (SIO)/Permalloy (Py) [32, 33], SIO/$Co_{1-x}Tb_x$ [34], and $SrRuO_3$/Co [35]. The resulting SOT efficiencies, $\xi_{||} \leq 1$ [32-35], are comparable to their HM/FM counterparts. With this as the background, our hypothesis was that creating atomically perfect ferromagnet and SOC metal layers, coupled through chemically abrupt epitaxial interfaces, can lead to emergent electronic phenomena at the interfaces [31], as well as the opportunity to obtain more efficient charge-to-spin conversion. For our studies, we chose the correlated perovskite manganite, $La_{0.7}Sr_{0.3}MnO_3$ (LSMO) and the SOC metal perovskite iridate, $SrIrO_3$ (SIO), as model systems.

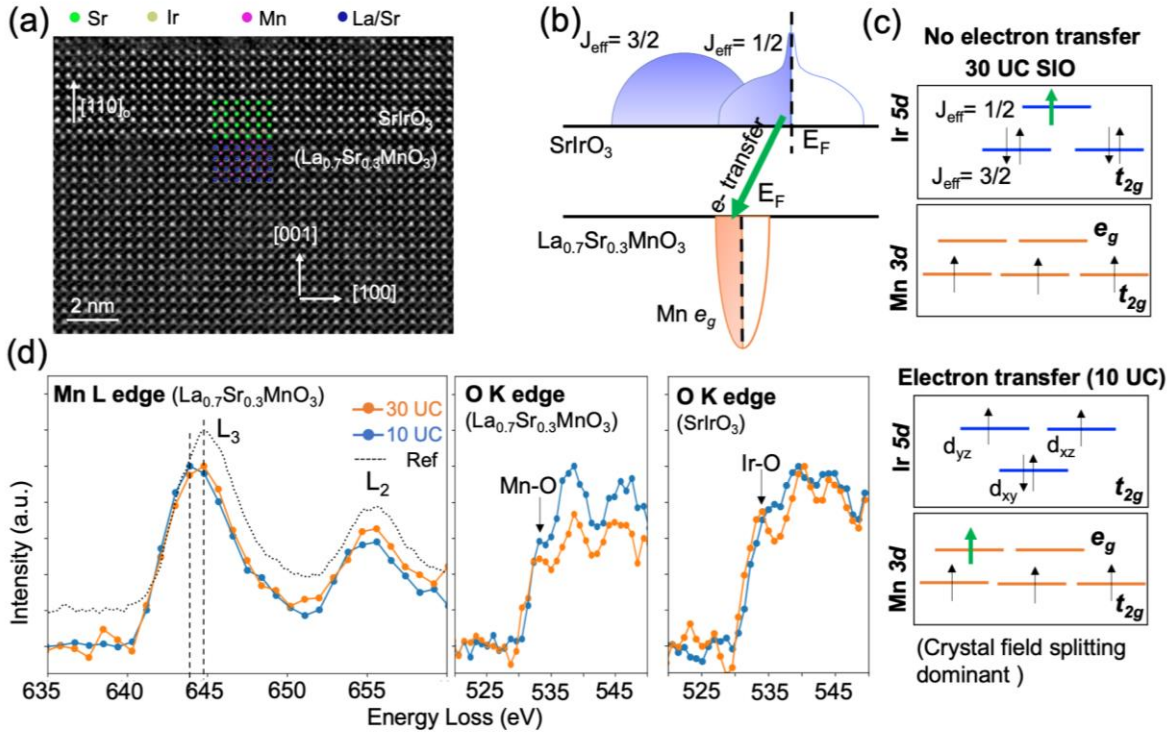


Figure 1|Local crystal and electronic structure of LSMO/SIO interface. a, High angle annular dark field (HAADF) image of LSMO/SIO layer displaying the atomically clean interface. b, The electronic arrangement of LSMO/SIO showing the electron charge transfer from $Ir^{4+}$ ($SrIrO_3$) to $Mn^{4+}$ ($La_{0.7}Sr_{0.3}MnO_3$). c, Orbital reconstruction of Mn 3d and Ir 5d levels for LSMO (50 UC)/SIO(10 UC) after the electron transfer. d, Mn L edge and O K edge EELS spectrum extracted from the LSMO/SIO interface for different thicknesses.

Epitaxial LSMO/SIO bilayers are grown on STO (0 0 1) substrates by high-pressure reflection high energy electron diffraction (RHEED)-assisted pulsed laser deposition. Sharp RHEED patterns (Fig. S1(a)) demonstrate high crystal quality and a flat surface. The thicknesses of LSMO and SIO layers are determined by counting periods of RHEED oscillations and confirmed by high resolution electron microscopy (HAADF-STEM). We verified by X-ray diffraction that high-quality, single-phase LSMO (50 UC)/SIO (25 UC) with the desired (0 0 1) orientation were grown on the STO (0 0 1) substrate (Fig. S2(a)). Fig. S2(b), (c), (d) show the reciprocal space maps of the STO//LSMO (50 UC)/SIO (25 UC) (0 0 3), (1 0 3), and (2 0 3) diffraction peaks, respectively, indicating that both LSMO and SIO are coherently strained to the STO substrate. Reciprocal space maps of the STO//LSMO (50 UC)/SIO (25 UC) around (1 0.5 1.5), (0.5 1 1.5) and (0.5 1.5 1) diffraction peaks are shown in Fig. S3(b), (c), (d), showing that the SIO layer presents domains with in-phase octahedral rotation axis aligned with both X and Y directions. No domains with in-phase octahedral rotation axis along Z are detected. In-phase octahedral rotations in the LSMO layer are not detected either.

To examine the quality of the oxide interface at the microscopic level, we performed high angle annular dark field (HAADF) scanning transmission electron microscopy (STEM) experiments (Fig. 1(a)). (Supplementary information, IV). The brighter contrast is from the SIO layer due to its higher $Z_{eff}$ whereas the darker contrast is from the LSMO layer. The sharp interface quality is evident from Fig. 1(a) with $MnO_2$ termination in LSMO and SrO termination in $SrIrO_3$.

From the XRD and HAADF-STEM experiments, we calculated the in-plane and out-of-plane (OOP) lattice parameters for the LSMO and SIO layers in heterostructures with varying SIO thicknesses. The results of these experiments are summarized in Supplementary information, III. Fig. S4(a) shows X-ray diffraction patterns of LSMO(50 UC)/SIO(X UC), where X=10, 20 and 30 unit cells; for each thickness, two separate samples were measured and were found to be essentially identical. The corresponding OOP lattice parameters are presented in the table in Fig. S4(b), along with the in-plane and OOP lattice parameter data extracted from the HAADF-STEM images of the 10 and 30UC SIO samples.

There are three key observations from this data. First, from the XRD data in Fig. S4(a), the LSMO OOP lattice parameter is essentially unchanged; second, the OOP lattice parameters of the SIO layer systematically change as a function of the SIO layer thickness, from 3.97 Å for the 10 UC SIO sample to 4.06 Å for the 30 UC SIO. We note that the SIO OOP lattice parameter (3.97 ± 0.02 Å) in the LSMO(50 UC)/SIO(10 UC) is smaller than what has been reported for 30 UC SIO grown on STO substrate (4.08 Å)[36]. Finally, more importantly, the OOP lattice parameter of the 30UC SIO on 50UC LSMO is essentially identical to that reported for the 30UC SIO on STO substrate[36]. Thus, pure relaxation of heteroepitaxial constraint imposed by the lattice mismatch between the in-plane dimensions of LSMO and SIO fails to explain the experimentally observed trend in OOP lattice dimensions in the SIO layer (i.e., the OOP lattice parameter of the SIO layer is changing counter to what would be expected from pure heteroepitaxial considerations). Fig. S4(c-f) capture the structural details of the STO/SIO(30 UC), STO/LSMO(50 UC) and the corresponding LSMO/SIO heterostructures with 10 and 30 UC of SIO.

Therefore, in order to throw more light onto this puzzling structural evolution with SIO thickness, we performed atomic resolution electron-energy loss spectroscopy (EELS) measurements, which probes the empty density of states as presented in Fig. 1(d). We observe a negative shift of ~1eV for the Mn L-edge in the 10UC SIO sample compared to the 30UC SIO sample (as well as the standard reference spectra[37] shown in Fig. 1(d)). These changes in the Mn L-edge point to the strong possibility of a charge transfer from Ir to Mn[38-40] shown in Fig. 1(b). We also observe a corresponding change in the O K-edge in the SIO layer (we note that we do not access the Ir L-edge, which appears at ~12KeV, and is not accessible in our EELS spectrometer). Since the EELS spectra essentially probes the empty density of states, the changes in the first 5eV of the O K-edge reflects changes in the electronic structure of the SIO layer, arising from changes in the Ir-O hybridization. Such a charge transfer can also be accompanied by orbital reconstruction in the SIO layer[31, 40]. Bulk SIO is a semimetal with strong spin-orbit coupling (SOC), which is comparable to the crystal field splitting (CFS) [41]. It has been recently reported that CFS can dominate over SOC in strained iridate systems [42]. An evidence for such an orbital re-construction due to CFS can be seen in O K edge in Fig. 1(d). In LSMO(50 UC)/SIO(10 UC), the density of states for Ir-O related levels are broader than that those in LSMO(50 UC)/SIO(30 UC). We believe that due to the dominance of CFS over the SOC, the S=1 state is stabilized in the LSMO(50 UC)/SIO(10 UC) as is shown in Fig. 1(c). Our present results agree with previously reported results on SrIrO3/LaNiO3 system[40]. We note that for LSMO(50 UC)/SIO(30 UC), where the charge transfer is negligible, there is no orbital reconstruction in Ir 5d levels shown in Fig. 1(c).

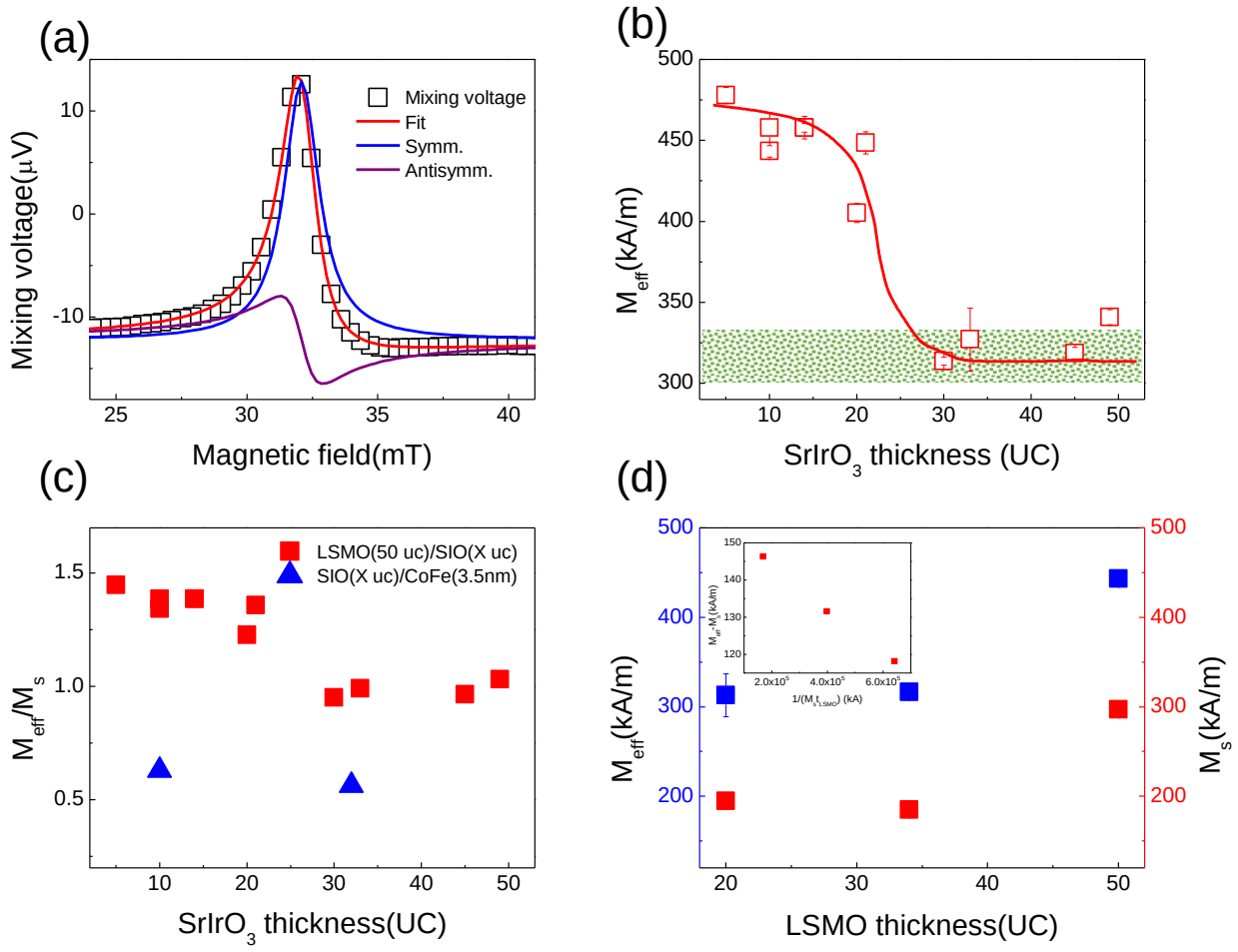


Figure 2 | ST-FMR and Effective Magnetization for LSMO/SIO bilayer. a, ST-FMR for sample LSMO (50 UC)/SIO (22 UC) at 4GHz. The external magnetic field is oriented at 45° with respect to the current direction. Open black squares indicate spin mixing voltage. The red line is a fit to the spin mixing voltage data while the blue and purple curves indicate extracted symmetric and anti-symmetric spin mixing voltages, respectively. b, Effective magnetization,$M_{\mathrm{eff}}$, extracted from ST-FMR measurements, for LSMO (50 UC)/SIO (X UC) as a function of SIO thickness. The green dotted band indicates the saturation magnetization, $M_{\mathrm{s}}$ (ranging from 300 to 330 kA/m), for 50 UC LSMO measured using vibrating sample magnetometry. The red solid line is a guide to illustrate the thickness dependent $M_{\mathrm{eff}}$ transition. c, The ratio of $M_{\mathrm{eff}}/M_{\mathrm{s}}$ as a function of SIO thickness. The red solid squares and blue solid triangles indicate LSMO (50 UC)/SIO (X UC), SIO (X UC)/CoFe (3.5 nm)/Al systems, respectively. d, $M_{\mathrm{eff}}$ and $M_{\mathrm{s}}$ for LSMO (X UC)/SIO (10 UC) as a function of LSMO thickness. The blue and red solid squares indicate $M_{\mathrm{eff}}$ and $M_{\mathrm{s}}$, respectively. The inset shows $M_{\mathrm{eff}}$ - $M_{\mathrm{s}}$ as a function of $1/(M_{\mathrm{s}}t_{\mathrm{LSMO}})$.

To understand the potential spintronic manifestations of the clean epitaxial LSMO/SIO interface and the resulting charge transfer and orbital reconstruction, ST-FMR measurements were performed on

LSMO/SIO heterostructures with varying thicknesses. The ST-FMR dc mixing voltage can be written as[43-45]:

$$V_{\mathrm{mix}} = -\frac{1}{4}\frac{\mathrm{dR}}{\mathrm{d}\Phi}\frac{\gamma \mathrm{I_{rf}}\cos\Phi}{\Delta 2\pi\left(\frac{\mathrm{df}}{\mathrm{dH}}\right)|H_{\mathrm{ext}}=\mathrm{H_0}}[SF_{\mathrm{S}}(H_{\mathrm{ext}}) + \mathrm{A}F_{\mathrm{A}}(H_{\mathrm{ext}})], \quad (1)$$

where $R(\Phi)$ is the device resistance as a function of the angle- $\Phi$ between the applied in-plane magnetic field and current direction, $\mathrm{I_{rf}}$ is the microwave current flowing into the device, $\left(\frac{\mathrm{df}}{\mathrm{dH}}\right)|H_{\mathrm{ext}} = \mathrm{H_0}$ is the field gradient of the resonance frequency, $F_{\mathrm{S}}(H_{\mathrm{ext}}) = {\Delta^2}/{\Delta^2 + (H_{\mathrm{ext}} - \mathrm{H_0})^2}$ is the symmetric Lorentzian function with half-width-half-maximum linewidth $\Delta$, $F_{\mathrm{A}}(H_{\mathrm{ext}}) = {(H_{\mathrm{ext}} - \mathrm{H_0})\Delta}/{\Delta^2 + (H_{\mathrm{ext}} - \mathrm{H_0})^2}$ is the anti-symmetric Lorentzian function. S and A are the amplitudes of the symmetric and anti-symmetric Lorentzian functions respectively. Fig. 2(a) shows an example ST-FMR measurement for LSMO (50 UC)/SIO (22 UC) at a frequency of 4 GHz and input power 18 dBm, with an external magnetic field oriented 45° to the current direction. The measured ST-FMR signal fits well to Eq. (1), yielding the symmetric and anti-symmetric components. The resonance fields are summarized in Fig. S10, and agree well with the Kittel equation:

$$f = \frac{\gamma}{2\pi}\sqrt{(\mu_0 H_{\mathrm{ext}} + \mu_0 H_{\mathrm{k}})(\mu_0 H_{\mathrm{ext}} + \mu_0 H_{\mathrm{k}} + \mu_0 M_{\mathrm{eff}})}\ , \quad (2)$$

where $H_{\mathrm{k}}$ is the in-plane magnetic field anisotropy. From the fit to Eq. (2), $M_{\mathrm{eff}}$ is extracted, showing a strong dependence on SIO thickness. As is shown in Fig. 2(b), a ~50% enhancement of effective magnetization compared to the bulk saturation magnetization (Supplementary information, VI, Fig. S7) is seen for LSMO (50 UC)/SIO (5 UC). The saturation magnetization $M_{\mathrm{S}}$ as measured by vibrating sample magnetometry does not show any such abrupt dependence on the SIO thickness (Fig. 2(b)), indicating that the enhancement of $M_{\mathrm{eff}}$ is likely due to a change in magnetic anisotropy. The enhancement in $M_{\mathrm{eff}}$ is observed only for SIO thinner than ~25 UC and progressively decreases for the thicker SIO samples. The enhancement of $M_{\mathrm{eff}}$ is observed for all LSMO thicknesses, confirming the universal role of SIO in enhancing the $M_{\mathrm{eff}}$ of LSMO. The effective magnetization can be written as $\mu_0 M_{\mathrm{eff}} = \mu_0 M_{\mathrm{S}} - H_{\mathrm{k,eff}}$ [46], where $H_{\mathrm{k,eff}}$ is the effective anisotropy field. This enhancement in $M_{\mathrm{eff}}$ in the epitaxial LSMO/SIO is quite different from the SIO/CoFe systems, see Fig. 2(c), which exhibits $M_{\mathrm{eff}} < M_{\mathrm{S}}$, and no strong dependence on SIO thickness, as typically seen in conventional metallic systems. This could be due to a difference in the sign of $H_{\mathrm{k,eff}}$ between the epitaxial LSMO/SIO and non-epitaxial SIO/Py, which further accentuates the peculiarity of the LSMO/SIO system. In conventional systems, $H_{\mathrm{k,eff}}$ can have contributions from a bulk component ($2K_{\mathrm{u}}/M_{\mathrm{S}}$) and an interface component ($2K_{\mathrm{int}}/M_{\mathrm{S}}t_{\mathrm{LSMO}}$) [46], where $K_{\mathrm{u}}$ and $K_{\mathrm{int}}$ are the bulk and interfacial anisotropy constants, respectively. The difference between $M_{\mathrm{eff}}$ and $M_s$ in the LSMO/SIO scales linearly with $1/M_{\mathrm{S}}t_{\mathrm{LSMO}}$, shown in the inset of Fig. 2(d), as expected from an interfacial contribution. ($M_{\mathrm{eff}} - M_{\mathrm{S}}$) vs $1/M_{\mathrm{S}}t_{\mathrm{LSMO}}$ shows a large intercept, suggesting a stronger contribution from bulk anisotropy; however, the trend suggests that the bulk and the interfacial anisotropies have opposite signs.

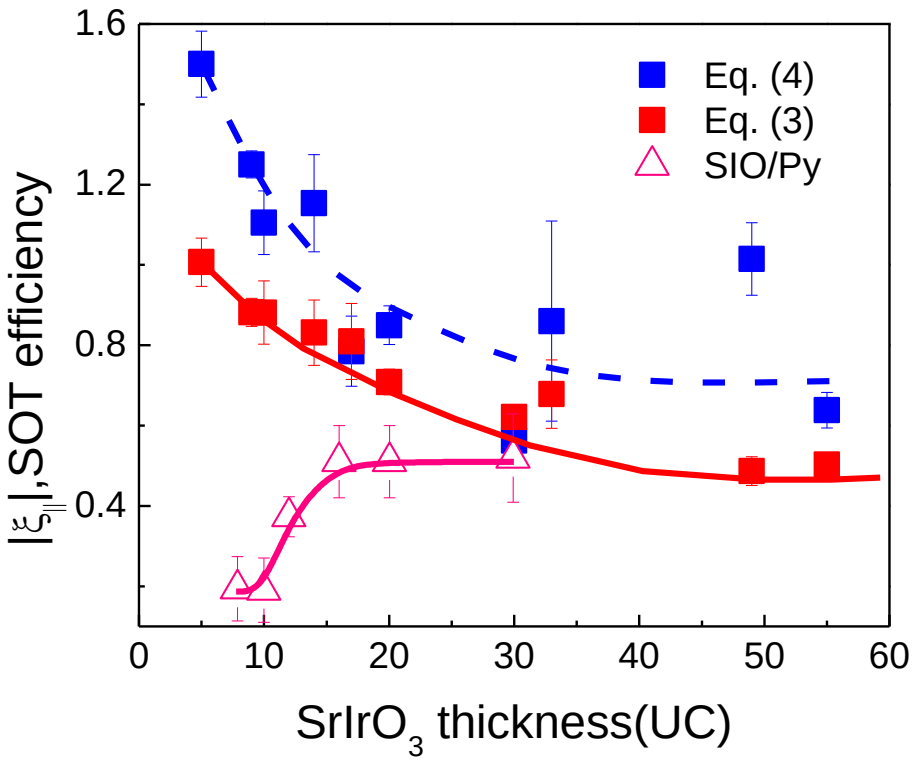


Figure 3|SOT Efficiency for LSMO/SIO. SOT efficiency as a function of SIO thickness is shown, with LSMO thickness fixed at 50 UC. The red solid squares represent SOT efficiency estimated by Eq. (3) for LSMO/SIO system. The red line is a guide to the eye. The blue solid squares indicate SOT efficiency for LSMO/SIO estimated by the modified Eq. (3)- $\xi_{||} = \frac{S}{A}(\frac{e}{\hbar})\mu_0 M_{eff} t_{FM} d_{NM} \sqrt{1 + {}^{\mu_0 M_{eff}}/_{H_0}}$ (4). The blue dashed line is a guide to the eye. The pink open triangles indicate SOT efficiency for SIO/Py[32]. The pink solid line is a guide for SIO/Py.

We now bring all the observed enhancements in $M_{eff}$ to focus by calculating the charge to spin conversion efficiency (SOT efficiency) from the ST-FMR measurements. We use the following expression to extract the SOT efficiencies as a function of SIO thickness:

$$\xi_{||} = \frac{S}{A}(\frac{e}{\hbar})\mu_0 M_S t_{FM} d_{NM} \sqrt{1 + {}^{\mu_0 M_{eff}}/_{H_0}} \quad (3)$$

Where $t_{FM}$ is the thickness of the FM, $d_{NM}$ is the thickness of the SOC material, and $H_0$ is the resonance field. Figure 3 summarizes the SOT efficiencies for LSMO/SIO as a function of SIO thickness, in which a strong dependence of SOT efficiency on SIO thickness is observed. As the SIO thickness increases, the SOT efficiency decays, in direct contrast to its non-epitaxial counterpart SIO/Py [32], whose SOT efficiency increases with SIO thicknesses and eventually saturates at ~0.5. The SOT efficiency saturation with SOC metal thickness is commonly attributed to spin diffusion length in the SOC material[47]. This contrasting thickness dependency suggests a distinctly different physics underlying the spin-charge conversion in these systems, resulting from the epitaxial interface. Further analyses on the effective interface spin

mixing conductance and interface transparency (Supplementary information, X) suggest that the enhancement of SOT efficiency is not simply due to the improvement of interface quality but is a result of the intrinsic electronic interaction (charge transfer + orbital reconstruction) between LSMO and SIO, supported by EELS mapping. Intriguingly, unlike traditional heavy-metal systems, $M_{\mathrm{eff}}$ is always equal to or larger than $M_{\mathrm{s}}$ in LSMO/SIO heterostructures, which brings into question the use of $M_{\mathrm{s}}$ in Eq. (3). Therefore, as a comparison, we have overlayed data in Fig. 3 (blue solid squares) where we have calculated $\xi_{||}$ using $M_{\mathrm{eff}}$ in the pre-factor rather than $M_{\mathrm{s}}$.

To rule out the presence of a substantial field like torque ($\xi_{\mathrm{FL}}$) in the LSMO/SIO system, we measured the ST-FMR as a function of LSMO thickness (Supplementary information, XI), which indicates a negligible $\xi_{\mathrm{FL}}$ ($\xi_{\mathrm{FL}}/\xi_{\mathrm{DL}} = -0.09$). To further validate the SOT efficiency estimated by ST-FMR, second harmonic Hall measurement for an exemplar LSMO (50 UC)/SIO (18 UC) sample (Supplementary information, XII) was performed and yields a $\xi_{\mathrm{DL}}$ of ~1.1, which is consistent with the ST-FMR value. These large SOT efficiencies, which show a ~3-5X enhancement over SIO/Py, and the distinct SIO thickness dependence directly point to the beneficial role of an epitaxial interface and novel physics accompanied by LSMO/SIO epitaxial interface.

We estimate the SOT conductivity ( $\sigma_{||}$ ) of our all-oxide device using $\xi_{||} = \sigma_{||}/\sigma$ to be roughly $1{\sim}3 \times 10^5(\frac{\hbar}{2e})\Omega^{-1} \cdot m^{-1}$. Note that the $\sigma_{||}$ in Pt is of the same order of magnitude [5, 48, 49], but it is achieved due to the product of a higher charge conductivity and a lower SOT efficiency. A high SOT efficiency in the epitaxial oxide heterostructure, such as LSMO/SIO is promising for a lower magnetization switching current with much lower current shunting (Supplementary information, VII). The most important observations in the epitaxial heterostructure are the key role of the electronic structure at the heteroepitaxial interface (Fig. 1) in enhancing the SOT efficiency, and how that electronic structure also induces a change in the anisotropy as measured in through the ST-FMR measurement through the enhancement in the $M_{\mathrm{eff}}$ relative to $M_{\mathrm{s}}$. Our preliminary theoretical studies (Supplementary information, XIII, XIV) confirm that this enhancement in $M_{\mathrm{eff}}$ is a consequence of additional anisotropy terms at thin SIO thicknesses. As also observed in the Pt/Co/Oxide heterostructures[50-53], we hypothesize that this is likely a result of electronic orbital hybridization and the associated charge transfer across the LSMO/SIO interface seen by the EELS data (Fig. 1). We also recognize that the electronic band structure can be influenced by the lattice parameter and crystal symmetry in addition to charge transfer effects. The key difference between the results presented in Fig.3 for the epitaxial LSMO/SIO interface and the SIO/Py interface[32] is the role of epitaxial constraints imposed on the crystal and electronic structure. We note that the SOT efficiency in our measurements for SIO layer thickness larger than ~25-30UC is essentially the same as that reported by T. Nan et al[32]. The significant enhancement occurs for SIO thicknesses smaller than ~25UC, for which the consequences of epitaxial constraint on the electronic and crystal structure are strongly manifested in the enhancement of the SOT efficiency. Untangling the complex interactions between the changes in crystal structure, lattice dimensions and electronic structure will require considerably more detailed experimental studies of the local crystal and electronic structure as a function of epitaxial constraint.

In summary, we use heteroepitaxial perovskite oxides driven by the intrinsic similarity in crystal chemistry and structure to design and synthesize epitaxial oxide FM/SOC metal heterostructures as model systems to study the SOT efficiency and novel interface-driven spin-orbitronics. Using ST-FMR, we report

heterostructures with $M_{\mathrm{eff}} > M_{\mathrm{s}}$ and $\xi_{||}$=1, taking advantage of intrinsic band structure and correlated electron phenomena. We show that precise control over crystallinity, crystal orientation, interface quality, and strain states of the bilayer, allows us to achieve high SOT efficiency with lower current shunting factor. The critical role of the interface electronic structure strongly suggests future work on manipulating the interface electronic structure through the insertion of "surfactant" layers that can locally manipulate the electronic structure. We anticipate that additional systematic temperature-dependent structural and electronic structure studies will elucidate and exploit more fundamental SOT physics in this system [31], emphasizing the significant role oxide epitaxy can play as a tool in spintronics. Furthermore, this work suggests a broader set of FM/SOC heterostructures that can be created using the principles of heteroepitaxy to yield large SOT efficiencies, given the rich diversity of oxide materials.

Acknowledgements: X.H., S.S., J.M., S.S., D.R., and R.R. acknowledge support from the SRC-JUMP ASCENT center. L.C. and H.Z., are supported by an AFOSR-MURI through Cornell University. L.C. acknowledges financial support from the University of California Office of the President and the Ford Foundation, administered through the National Academy of Sciences. F.M., Q. S., and N.K. acknowledge support from NSF ERC-TANMS Grant No. 1160504 and NSF-PREM Grant No. DMR-1828019. The electron microscopy experiments were performed at the Molecular Foundry, Lawrence Berkeley National Laboratory, which is supported by the U.S. Department of Energy under contract no. DE-AC02-05CH11231. S.S. is supported by the DOE EFRC on Quantum Coherence. S.K. is supported by the DOE (DE-SC0017671). V.A.S. acknowledges support from the US Department of Energy Office of Science-Basic Energy Sciences, under Award Number DE-SC-0012375 for the development of the materials and synchrotron-based study of ferroic thin films. V.A.S. would like to thank to Evguenia Karapetrova and Zhan Zhang for their support in performing the experiments at the beamlines 33-BM-C and 33-ID-D from Advanced Photon Source, Argonne National Laboratory. This research used resources of the Advanced Photon Source, a US Department of Energy (DOE) Office of Science User Facility, operated for the DOE Office of Science by Argonne National Laboratory under Contract No. DE-AC02-06CH11357. Extraordinary facility operations were supported in part by the DOE Office of Science through the National Virtual Biotechnology Laboratory, a consortium of DOE national laboratories focused on the response to COVID-19, with funding provided by the Coronavirus CARES Act.

## Figure Captions

Figure 1|Local crystal and electronic structure of LSMO/SIO interface. a, High angle annular dark field (HAADF) image of LSMO/SIO layer displaying the atomically clean interface. b, The electronic arrangement of LSMO/SIO showing the electron charge transfer from $Ir^{4+}$ ($SrIrO_3$) to $Mn^{4+}$ ($La_{0.7}Sr_{0.3}MnO_3$). c, Orbital reconstruction of Mn 3d and Ir 5d levels for LSMO (50 UC)/SIO(10 UC) after the electron transfer. d, Mn L edge and O K edge EELS spectrum extracted from the LSMO/SIO interface for different thicknesses.

Figure 2 | ST-FMR and Effective Magnetization for LSMO/SIO bilayer. a, ST-FMR for sample LSMO (50 UC)/SIO (22 UC) at 4GHz. The external magnetic field is oriented at 45° with respect to the current direction. Open black squares indicate spin mixing voltage. The red line is a fit to the spin mixing voltage data while the blue and purple curves indicate extracted symmetric and anti-symmetric spin mixing voltages, respectively. b, Effective magnetization,$M_{\mathrm{eff}}$, extracted from ST-FMR measurements, for LSMO (50 UC)/SIO (X UC) as a function of SIO thickness. The green dotted band indicates the saturation magnetization, $M_{\mathrm{s}}$, for 50 UC LSMO measured using vibrating sample magnetometry. The solid red line is a guide to illustrate the thickness dependent $M_{\mathrm{eff}}$ transition. c, The ratio of $M_{\mathrm{eff}}/M_{\mathrm{s}}$ as a function of SIO thickness. The red solid squares and blue solid triangles indicate LSMO (50 UC)/SIO (X UC), SIO (X UC)/CoFe (3.5 nm)/Al systems, respectively. d, $M_{\mathrm{eff}}$ and $M_{\mathrm{s}}$ for LSMO (X UC)/SIO (10 UC) as a function of LSMO thickness. The blue and red solid squares indicate $M_{\mathrm{eff}}$ and $M_{\mathrm{s}}$, respectively. The inset shows $M_{\mathrm{eff}}$ - $M_{\mathrm{s}}$ as a function of $1/(M_{\mathrm{s}}t_{\mathrm{LSMO}})$.

Figure 3|SOT Efficiency for LSMO/SIO. SOT efficiency as a function of SIO thickness is shown, with LSMO thickness fixed at 50 UC. The red solid squares represent SOT efficiency estimated by Eq. (3) for LSMO/SIO system. The red line is a guide to the eye. The blue solid squares indicate SOT efficiency for LSMO/SIO estimated by the modified Eq. (3)- $\xi_{||} = \frac{\mathrm{S}}{\mathrm{A}}(\frac{\mathrm{e}}{\hbar})\mu_0 M_{\mathrm{eff}} \mathrm{t_{FM}} \mathrm{d_{NM}} \sqrt{1 + {}^{\mu_0 M_{\mathrm{eff}}}/_{\mathrm{H_0}}}$ (4). The blue dashed line is a guide to the eye. The pink open triangles indicate SOT efficiency for SIO/Py[32]. The pink solid line is a guide for SIO/Py.

## References


[1] P. Gambardella and I. M. Miron, Philos. Trans. A Math Phys. Eng. Sci. 2011, **369**, 3175.
[2] T. Jungwirth, X. Marti, P. Wadley and J. Wunderlich, Nat. Nanotechnol. 2016, **11**, 231.
[3] Y. Otani, M. Shiraishi, A. Oiwa, E. Saitoh and S. Murakami, Nat. Phys. 2017, **13**, 829.
[4] A. Manchon and S. Zhang, Phys. Rev. B 2009, **79**, 094422.
[5] I. M. Miron, K. Garello, G. Gaudin, P. J. Zermatten, M. V. Costache, S. Auffret, S. Bandiera, B. Rodmacq, A. Schuhl and P. Gambardella, Nature 2011, **476**, 189.
[6] L. Liu, C.-F. Pai, Y. Li, H. W. Tseng, D. C. Ralph and R. A. Buhrman, Science 2012, **336**, 555.
[7] A. Manchon, H. C. Koo, J. Nitta, S. M. Frolov and R. A. Duine, Nat. Mater. 2015, **14**, 871.
[8] M. B. Jungfleisch, W. Zhang, J. Sklenar, W. Jiang, J. E. Pearson, J. B. Ketterson and A. Hoffmann, Phys. Rev. B 2016, **93**, 224419.
[9] H. Wu, P. Zhang, P. Deng, Q. Lan, Q. Pan, S. A. Razavi, X. Che, L. Huang, B. Dai, K. Wong, X. Han and K. L. Wang, Phys. Rev. Lett. 2019, **123**, 207205.
[10] K. Ando, S. Takahashi, K. Harii, K. Sasage, J. Ieda, S. Maekawa and E. Saitoh, Phys. Rev. Lett. 2008, **101**, 036601.
[11] J. Kim, J. Sinha, M. Hayashi, M. Yamanouchi, S. Fukami, T. Suzuki, S. Mitani and H. Ohno, Nat. Mater. 2013, **12**, 240.
[12] X. Fan, J. Wu, Y. Chen, M. J. Jerry, H. Zhang and J. Q. Xiao, Nat. Commun. 2013, **4**, 1799.
[13] S. Emori, U. Bauer, S. M. Ahn, E. Martinez and G. S. Beach, Nat. Mater. 2013, **12**, 611.
[14] Y. Wang, P. Deorani, K. Banerjee, N. Koirala, M. Brahlek, S. Oh and H. Yang, Phys. Rev. Lett. 2015, **114**, 257202.
[15] H. Zhang, C.-X. Liu, X.-L. Qi, X. Dai, Z. Fang and S.-C. Zhang, Nat. Phys. 2009, **5**, 438.
[16] Y. Fan, P. Upadhyaya, X. Kou, M. Lang, S. Takei, Z. Wang, J. Tang, L. He, L. T. Chang, M. Montazeri, G. Yu, W. Jiang, T. Nie, R. N. Schwartz, Y. Tserkovnyak and K. L. Wang, Nat. Mater. 2014, **13**, 699.
[17] A. R. Mellnik, J. S. Lee, A. Richardella, J. L. Grab, P. J. Mintun, M. H. Fischer, A. Vaezi, A. Manchon, E. A. Kim, N. Samarth and D. C. Ralph, Nature 2014, **511**, 449.
[18] Q. Song, H. Zhang, T. Su, W. Yuan, Y. Chen, w. Xing, J. Shi, j. Sun and W. Han, Sci. Adv. 2017, **3**, e1602312.
[19] E. Lesne, Y. Fu, S. Oyarzun, J. C. Rojas-Sanchez, D. C. Vaz, H. Naganuma, G. Sicoli, J. P. Attane, M. Jamet, E. Jacquet, J. M. George, A. Barthelemy, H. Jaffres, A. Fert, M. Bibes and L. Vila, Nat. Mater. 2016, **15**, 1261.
[20] H. Zhang, Y. Ma, H. Zhang, X. Chen, S. Wang, G. Li, Y. Yun, X. Yan, Y. Chen, F. Hu, J. Cai, B. Shen, W. Han and J. Sun, Nano Lett. 2019, **19**, 1605.
[21] P. Laczkowski, Y. Fu, H. Yang, J. C. Rojas-Sánchez, P. Noel, V. T. Pham, G. Zahnd, C. Deranlot, S. Collin, C. Bouard, P. Warin, V. Maurel, M. Chshiev, A. Marty, J. P. Attané, A. Fert, H. Jaffrès, L. Vila and J. M. George, Phys. Rev. B 2017, **96**, 140405(R).
[22] K. U. Demasius, T. Phung, W. Zhang, B. P. Hughes, S. H. Yang, A. Kellock, W. Han, A. Pushp and S. S. P. Parkin, Nat. Commun. 2016, **7**, 10644.
[23] J. Han, A. Richardella, S. A. Siddiqui, J. Finley, N. Samarth and L. Liu, Phys. Rev. Lett. 2017, **119**, 077702.
[24] Y. Wang, D. Zhu, Y. Wu, Y. Yang, J. Yu, R. Ramaswamy, R. Mishra, S. Shi, M. Elyasi, K. L. Teo, Y. Wu and H. Yang, Nat. Commun. 2017, **8**, 1364.
[25] E. Dagotto, in *Nanoscale phase separation and colossal magnetoresistance*, 2003.
[26] N. A. Spaldin and R. Ramesh, Nat. Mater. 2019, **18**, 203.

[27] J. H. Haeni, P. Irvin, W. Chang, R. Uecker, P. Reiche, Y. L. Li, S. Choudhury, W. Tian, M. E. Hawley, B. Craigo, A. K. Tagantsev, X. Q. Pan, S. K. Streiffer, L. Q. Chen, S. W. Kirchoefer, J. Levy and D. G. Schlom, Nature 2004, **430**, 758.
[28] X.-L. Qi and S.-C. Zhang, Rev. Mod. Phys. 2011, **83**, 1057.
[29] M. Konig, S. Wiedmann, C. Brune, A. Roth, H. Buhmann, L. W. Molenkamp, X.-L. Qi and S.-C. Zhang, Science 2007, **318**, 766.
[30] N. P. Armitage, E. J. Mele and A. Vishwanath, Rev. Mod. Phys. 2018, **90**, 015001.
[31] D. Yi, J. Liu, S. L. Hsu, L. Zhang, Y. Choi, J. W. Kim, Z. Chen, J. D. Clarkson, C. R. Serrao, E. Arenholz, P. J. Ryan, H. Xu, R. J. Birgeneau and R. Ramesh, PNAS 2016, **113**, 6397.
[32] T. Nan, T. J. Anderson, J. Gibbons, K. Hwang, N. Campbell, H. Zhou, Y. Q. Dong, G. Y. Kim, D. F. Shao, T. R. Paudel, N. Reynolds, X. J. Wang, N. X. SUN, E. Y. Tsymbal, S. Y. Choi, M. S. Rzchowski, Y. B. Kim, D. C. Ralph and C. B. Eom, PNAS 2019, **116**, 16186.
[33] A. S. Everhardt, M. Dc, X. Huang, S. Sayed, T. A. Gosavi, Y. Tang, C.-C. Lin, S. Manipatruni, I. A. Young, S. Datta, J.-P. Wang and R. Ramesh, Phys. Rev. Mater. 2019, **3**, 051201.
[34] H. Wang, K.-Y. Meng, P. Zhang, J. T. Hou, J. Finley, J. Han, F. Yang and L. Liu, Appl. Phys. Lett. 2019, **114**, 232406.
[35] Y. Ou, Z. Wang, C. S. Chang, H. P. Nair, H. Paik, N. Reynolds, D. C. Ralph, D. A. Muller, D. G. Schlom and R. A. Buhrman, Nano Lett. 2019, **19**, 3663.
[36] D. J. Groenendijk, N. Manca, G. Mattoni, L. Kootstra, S. Gariglio, Y. Huang, E. van Heumen and A. D. Caviglia, Appl. Phys. Lett. 2016, **109**, 041906.
[37] P. Ewels, T. Sikora, V. Serin, C. P. Ewels and L. Lajaunie, Microsc. Microanal. 2016, **22**, 717.
[38] J. Nichols, X. Gao, S. Lee, T. L. Meyer, J. W. Freeland, V. Lauter, D. Yi, J. Liu, D. Haskel, J. R. Petrie, E. J. Guo, A. Herklotz, D. Lee, T. Z. Ward, G. Eres, M. R. Fitzsimmons and H. N. Lee, Nat. Commun. 2016, **7**, 12721.
[39] S. Okamoto, J. Nichols, C. Sohn, S. Y. Kim, T. W. Noh and H. N. Lee, Nano Lett. 2017, **17**, 2126.
[40] X. Liu, M. Kotiuga, H. S. Kim, A. T. N'Diaye, Y. Choi, Q. Zhang, Y. Cao, M. Kareev, F. Wen, B. Pal, J. W. Freeland, L. Gu, D. Haskel, P. Shafer, E. Arenholz, K. Haule, D. Vanderbilt, K. M. Rabe and J. Chakhalian, PNAS 2019, **116**, 19863.
[41] M. A. Zeb and H.-Y. Kee, Phys. Rev. B 2012, **86**, 085149.
[42] X. Liu, V. M. Katukuri, L. Hozoi, W. G. Yin, M. P. Dean, M. H. Upton, J. Kim, D. Casa, A. Said, T. Gog, T. F. Qi, G. Cao, A. M. Tsvelik, J. van den Brink and J. P. Hill, Phys. Rev. Lett. 2012, **109**, 157401.
[43] L. Liu, T. Moriyama, D. C. Ralph and R. A. Buhrman, Phys. Rev. Lett. 2011, **106**, 036601.
[44] J. C. Sankey, P. M. Braganca, A. G. Garcia, I. N. Krivorotov, R. A. Buhrman and D. C. Ralph, Phys. Rev. Lett. 2006, **96**, 227601.
[45] H. Kubota, A. Fukushima, K. Yakushiji, T. Nagahama, S. Yuasa, K. Ando, H. Maehara, Y. Nagamine, K. Tsunekawa, D. D. Djayaprawira, N. Watanabe and Y. Suzuki, Nat. Phys. 2007, **4**, 37.
[46] A. Conca, A. Niesen, G. Reiss and B. Hillebrands, AIP Adv. 2019, **9**, 085205.
[47] F. Mahfouzi, R. Mishra, P.-H. Chang, H. Yang and N. Kioussis, Phys. Rev. B 2020, **101**, 060405.
[48] L. Liu, O. J. Lee, T. J. Gudmundsen, D. C. Ralph and R. A. Buhrman, Phys. Rev. Lett. 2012, **109**, 096602.
[49] M. H. Nguyen, D. C. Ralph and R. A. Buhrman, Phys. Rev. Lett. 2016, **116**, 126601.
[50] S. Monso, Appl. Phys. Lett. 2002, **80**, 4157.
[51] N. Nakajima, T. Koide, T. Shidara, H. Miyauchi, H. Fukutani, A. Fujimori, K. Lio, T. Katayama, M. Nyvlt and Y. Suzuki, Phys. Rev. Lett. 1998, **81**, 5229.
[52] K. Kyuno, R. Yamamoto and S. Asano, J. Phys, Soc. Jpn. 1992, **61**, 2099.
[53] D. Weller, Y. Wu, J. Stohr, M. G. Samant, B. D. Hermsmeier and C. Chappert, Phys. Rev. B. 1994, **49**, 12888.